nature communications

Article

https://doi.org/10.1038/s41467-025-56692-2

Volcanically forced Madden–Julian oscillation triggers the immediate onset of El Niño

Received: 18 July 2023

Accepted: 28 January 2025

Published online: 06 February 2025

Check for updates

Hyemi Kim [1,2] ✉, Seung-Ki Min [3,4] ✉, Daehyun Kim [5,6] & Daniele Visioni [7]

A process-level understanding of the volcanically forced climate response is an urgent challenge due to its similarities to the potential effects of geoengineering techniques. Although the influence of volcanic forcing on El Niño events has been studied extensively, the mechanisms driving the volcanically-induced immediate onset of El Niño remain uncertain, with many climate models producing a delayed El Niño response compared to observations. In this study, using large ensemble simulations that allow us to isolate the impacts of volcanic forcing on the El Niño response, we demonstrate a mechanism that highlights the central triggering role of the Madden–Julian oscillation (MJO), which has been overlooked in existing literature. Because the land areas surrounding the Indo-Pacific warm pool dry more quickly after a volcanic eruption, the background moisture distribution becomes more favorable for the MJO to propagate eastward from the Indian Ocean into the Pacific. This increases the likelihood of ensemble members having stronger MJO activity in the western Pacific by about 35% compared to non-volcanic years, which subsequently increases the frequency of westerly wind bursts by about 76%, ultimately enhancing the probability of the onset of an El Niño by about 98% following major volcanic eruptions.

On 15th January 2022, the explosive eruption of Hunga Tonga-Hunga Ha'apai injected the highest amount of water vapor into the stratosphere, rivaling the explosiveness of the Pinatubo eruption in 1991[1]. It caused an estimated US$90.4 million in damages due to the effects of the resulting tsunami and ashfall[2]. Volcanic eruptions (VEs), such as the Pinatubo eruption, would impact not only economies but also regional and global climates, as well as their seasonal predictability[3]. Volcanic eruptions are a dominant form of external forcing that significantly affects the climate by injecting dust particles and sulfur dioxide into the atmosphere[4]. As sulfur moves into the stratosphere, it combines with water and forms sulfate aerosols that reflect incoming shortwave solar radiation. Because it takes a few years for these sulfate aerosols to settle out of the atmosphere, they cool the Earth's surface worldwide during this period. For example, the Mt. Pinatubo eruption in June 1991 cooled the global surface by a few tenths of a degree Celsius over about three years and led to a substantial decrease in global streamflow and land precipitation, as less shortwave radiation reached the surface, thereby reducing evaporation and stabilizing the atmosphere[5].

In addition to its significant impact on the mean climate, VEs are also known to affect natural modes of climate variability, such as the El Niño-Southern Oscillation (ENSO), the dominant mode of tropical interannual variability. However, no consensus has yet been reached on the immediate ENSO response to volcanic forcing, complicating the

[1]Department of Science Education, Ewha Womans University, Seoul, Republic of Korea. [2]School of Marine and Atmospheric Sciences, Stony Brook University, New York, US. [3]Division of Environmental Science and Engineering, Pohang University of Science and Technology, Pohang, Republic of Korea. [4]Institute for Convergence Research and Education in Advanced Technology, Yonsei University, Incheon, Republic of Korea. [5]School of Earth and Environmental Sciences, Seoul National University, Seoul, Republic of Korea. [6]Department of Atmospheric and Climate Science, University of Washington, Seattle, WA, USA. [7]Department of Earth and Atmospheric Sciences, Cornell University, Ithaca, NY, USA. ✉e-mail: hyemi.kim@ewha.ac.kr; skmin@postech.ac.kr

current understanding of ENSO dynamics[6–17]. Using targeted experiments with global climate models (GCMs), most studies have reported El Niño-like responses to volcanic forcing[10], though La Niña-like responses and no significant responses have been reported as well[11,12]. Anomalous westerly winds over the western Pacific have often been proposed as an important driver of the El Niño events that develop after a VE in simulations. That is, the volcanically forced radiative cooling and drying occur faster over the land areas than the ocean, especially over the Maritime Continent (MC) and surrounding area, and the increased land-ocean temperature gradient weakens the equatorial Walker circulation and enhances westerly anomalies in the western Pacific, inducing El Niño[13–17] through the Bjerknes feedback[18]. The cooling and reduction of precipitation over northern Africa are also thought to be a major source of an altered Walker circulation after volcanic eruption[16,17]. However, this mechanism has not been supported by a wider variety of models and, more importantly, produces delayed El Niño responses with a peak during the year after eruptions, which fails to explain the observed immediate onset of El Niño. While the volcanically forced changes in tropical westerly wind is known to be crucial for El Niño onset, the proposed mechanisms are still debated.

It has been widely accepted that the westerly anomalies associated with weaker Walker circulation consist of a series of short-lived, intense, and low-level westerly wind events that are referred to as westerly wind bursts (WWBs)[19]. WWBs are often associated with large clusters of deep convective clouds[20] and are recognized as precursors to El Niño events because they excite downwelling oceanic Kelvin waves[21]. In particular, when ENSO is in a neutral phase, El Niño can be strongly influenced by WWBs[19]. For example, an increase in WWB activity was observed prior to the 1982/83 and 1991/92 El Niño events[21,22], which occurred in conjunction with two major tropical volcanic eruptions, El Chichón (1982) and Mt. Pinatubo (1991).

The extent to which WWBs associated with deep convective clusters contribute to the immediate onset of an El Niño event within a few months after a volcanic eruption remains unexplored, as previous studies[17,23] have relied only on monthly or seasonally averaged wind data, in which the high-frequency signals of WWBs were averaged out. In the present study, we use daily data to determine the possible influence of volcanic-forced high-frequency WWBs on El Niño through their connection with the Madden–Julian oscillation (MJO). The MJO is the dominant mode of tropical intraseasonal variability and is characterized by an eastward-propagating, large-scale envelope of deep convective clusters that is strongly coupled with circulation anomalies[24]. After beginning its life cycle over the Indian Ocean, the MJO reaches the western Pacific if it survives the barrier effect of the Maritime Continent. In the western Pacific, studies have found that the strongest, longest-lasting, basin-scale WWBs were mostly associated with active MJO events[19,25–28]. These MJO-driven WWBs in the western Pacific then increase sea surface temperatures (SST) in the eastern Pacific by a few tenths of a degree Celsius[28]. Therefore, if MJO activity is enhanced over the western Pacific, the likelihood of MJO-driven WWB occurrence increases, eventually facilitating the subsequent development of an El Niño event. This hypothesis is tested in this study by proposing a plausible mechanism using reanalysis data and climate model sensitivity experiments. It is important to note that the role of volcanically forced MJO on ENSO has been overlooked in existing literature.

To test the hypothesis by isolating the volcanic forcing from other external forcings, single-forcing large ensemble experiments (SE) are utilized (see Methods for details). High model fidelity in simulating the observed climate is essential to accurately quantify the impact of forced signals on climate variability. However, many GCMs struggle with systematic biases. For example, while El Niño immediately peaks in the first winter following the major tropical volcanic eruption in reconstructions and observations[10], most GCMs simulate the El Niño peak during the second or third winter[13,15,17,29], limiting confidence in the proposed mechanisms. The present study seeks to partly resolve the issue by utilizing the Community Earth System Model Version 2.0 (CESM2) which is one of the few contemporary climate models that can realistically simulate both the ENSO and MJO[30–34]. In particular, as demonstrated later, the timing of the El Niño onset after volcanic forcing (i.e., the first winter following an eruption) is captured well by the CESM2, unlike most other GCMs. This accurate simulation of response timing is a necessary condition for better understanding the underlying mechanism.

Results

Volcanically forced responses of ENSO, MJO, and WWBs

This study focuses on two recent VEs: El Chichón in April 1982 and Mt. Pinatubo in June 1991. Fig. 1 presents the observed temporal changes in the monthly indices of Niño 3.4, MC moisture, MJO activity, and WWB frequency after the two VEs. The observations reveal that both VEs lead to the drying of MC moisture, which reached a minimum 6–7 months after the eruption (Fig. 1A). As documented in previous studies, El Niño intensified immediately after the two VE events and reached a peak after about 7–9 months. However, this immediate onset is not simulated in most GCMs. Before the El Niño maximum phase, in conjunction with the enhanced MJO activity over the western Pacific (Fig. 1B), the WWB frequency increases in the western Pacific before dropping sharply after about 7 months, with MJO activity also suppressed (Fig. 1C). These results suggest that an increase in MJO activity over the western Pacific is associated with WWB activity, and it may have contributed to the rapid development of an El Niño event immediately after the recent large VEs.

The spatial pattern of moisture (defined as column-integrated water vapor) 3–7 months after the VEs exhibits significant negative anomalies near the MC and positive moisture anomalies in the central to eastern tropical Pacific (Fig. 2A and B), which is consistent with previous studies[15]. Regarding the African drying mechanism[16,17], the observed moisture pattern shows a less consistent and weaker response than the MC drying. During the same period, MJO activity is suppressed in the vicinity of the MC and significantly enhanced in the western to central Pacific, with the maximum near the dateline (Fig. 2C and D). The similar changes in moisture and MJO activity anomalies before the peak phase of El Niño suggest that there could be a plausible link between the moisture and MJO after recent VEs.

By fully utilizing all ensemble members in the CESM2-SE and CESM2-LE, we assess the degree to which changes in MC moisture and MJO activity are volcanically forced responses. Supplementary Fig. 1 presents the probability distribution of normalized monthly MC moisture and MJO activity indices for the 3–7 month window after two VE years and nonVE years. About 35% of the ensembles simulate anomalously strong MC drying (defined as less than -1.0σ of the index) in VE years that is about twice as high as that for the nonVE years (17.8%) (Supplementary Fig. 1A). During the same period, the likelihood of MJO activity being anomalously strong (larger than $+1.0\sigma$) in VE years increases by about 36% compared with the corresponding values for the nonVE years (Supplementary Fig. 1B). Furthermore, using the $+1.0\sigma$ threshold for the 3–7 month window, the westerly wind stress (TAUx) index over the western Pacific increases by about 62% (Supplementary Fig. 1C) and WWBs frequency increases by 76% during VE years. Eventually, the chance of being strong El Niño (defined as greater than $+1.0\sigma$ of Niño 3.4 index) increases by about 98% after volcanic eruptions (Supplementary Fig. 1D). To further verify the robustness of the results, the same analysis is performed with 100 ensemble members of CESM2-LE, and although the signals are weaker, the responses are generally similar to CESM2-SE (Supplementary Fig. 2). These results indicate that the observed MC drying and enhanced western Pacific MJO activity are robust responses to large volcanic forcing and suggest a possible link with WWBs and ENSO.

https://doi.org/10.1038/s41467-025-56692-2

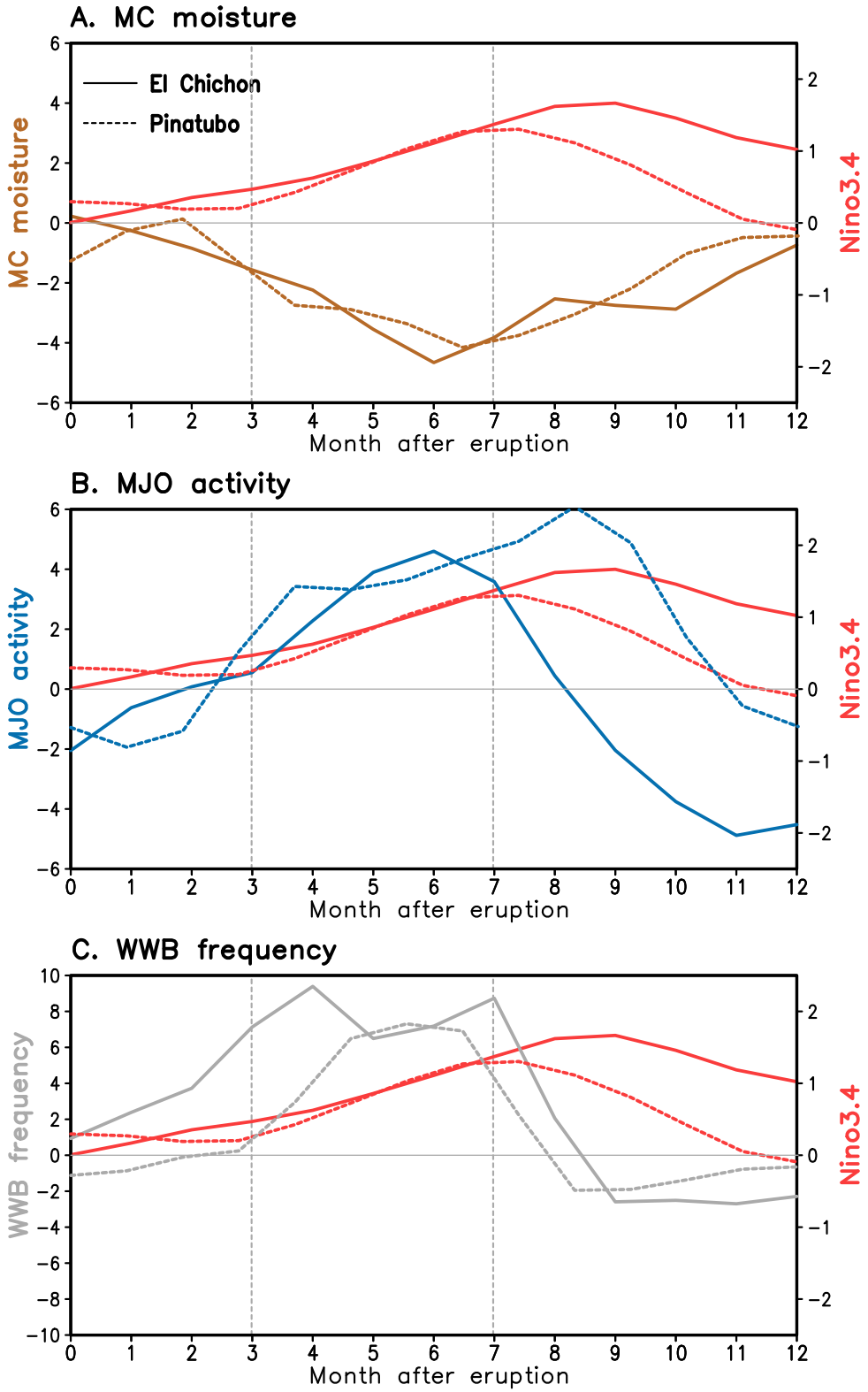


Fig. 1 | Observed temporal changes in the indices after two Volcanic Eruptions (VEs). Averaged monthly time series of anomalous (**A**) Maritime Continent (MC) moisture, (**B**) Madden–Julian oscillation (MJO) activity, and (**C**) westerly wind bursts (WWB) frequency indices (left *y*-axis) along with the Niño 3.4 index (red line, right *y*-axis) after two VEs: El Chichón (solid line) and Mt. Pinatubo (dashed line). Month 0 indicates the pre-eruption month, and the dashed vertical lines indicate 3 and 7 months after the eruption. A nine-point smoothing is applied to the time series.

https://doi.org/10.1038/s41467-025-56692-2

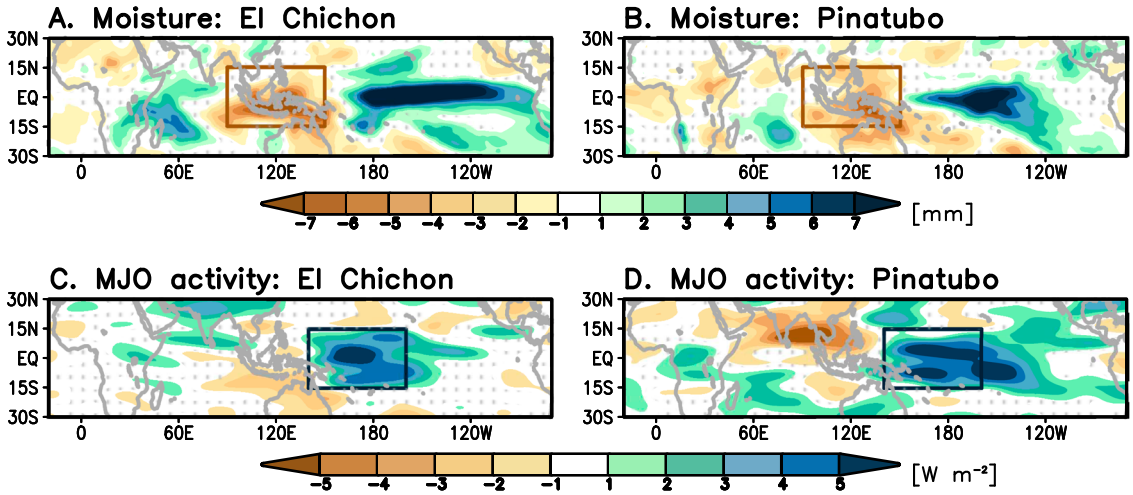


Fig. 2 | Observed anomalous moisture and Madden-Julian oscillation (MJO) activity after two Volcanic Eruptions (VEs). A, **B** Anomalous moisture and (**C**, **D**) MJO activity averaged over a window of 3–7 months after the El Chichón and Mt. Pinatubo eruptions. The brown and blue boxes indicate areas defined for the Maritime Continent (MC) moisture index (90°E–150°E, 15°S–15°N) and the MJO activity index (140°E–200°E, 15°S–15°N), respectively. The areas without stippling marks where the anomalies are statistically significant at the 99% confidence level based on two-sided *t* tests.

While comparing the full ensembles between VE and nonVE years offers an opportunity to understand forced responses in a probabilistic manner (Supplementary Figs. 1 and 2), averaging over all ensemble members may underestimate the magnitude of internal variability, as different ensemble members are in various climate states at the time of a volcanic eruption. To further clarify the mechanisms responsible for the volcanically forced MJO and ENSO, we cluster ensemble members based on their ENSO phase similar to that observed in the pre-eruption month (month 0). Sea surface height (SSH) anomaly, which is a proxy for ocean heat variation in the Pacific, is used for ensemble clustering (see "Methods"). We examine the response of the MC moisture, MJO activity, TAUx, WWB frequency, and ENSO to two major VE forcings in CESM2-SE using ensemble members that have similar ENSO states (neutral state) to that observed at month 0 and compare the composites of ensemble members to the corresponding nonVE clusters (Fig. 3). ENSO started with an initially neutral state, and about three months after the VE, an El Niño event develops and becomes significantly different from the nonVE clusters (Fig. 3A and Supplementary Fig. 3). Although somewhat weaker than the observed as the signal from each ensemble member is averaged out, the peak in the El Niño event appears about 6-7 months after the VE which roughly corresponds with observations (Fig. 1). This demonstrates that volcanic forcing can significantly influence El Niño development without a pre-existing El Niño signal at the time of the eruption. More importantly, while most GCMs simulate the peak of the El Niño event in the second or third winter[13,15,17,29], the CESM2-SE successfully reproduces the observed El Niño timing, thus providing higher confidence for the estimated forced response of the ENSO and related physical mechanism.

In conjunction with the pre-eruption neutral ENSO phase, the moisture anomaly over the MC is nearly zero at month 0 for both the VE and nonVE clusters (Fig. 3A). Supplementary Fig. 3 shows the composite difference between VE and nonVE clusters for the September-October-November (SON) averaged field. The MC moisture becomes significantly drier than the nonVE, again similar to the observed response (Fig. 3A and Supplementary Fig. 3A). Note that the moisture patterns (Supplementary Fig. 3A) are similar in two VE events. Synchronized changes of MJO activity (Fig. 3A and Supplementary Fig. 3B), enhanced westerly wind stress (TAUx), increased WWB frequency, and El Niño signal after the VE are also visible (Fig. 3A, B and Supplementary Fig. 3C, D), exhibiting significant differences from the nonVE cluster. For example, the WWB frequency during VE is about twice as high as in the nonVE cluster as the MJO activity enhances in 3 months after the VE. The MJO activity, TAUx, and WWB frequency escalate as the MC drying signal becomes robustly consistent with the observed signal, suggesting that volcanically forced MC drying enhances the MJO activity and westerly wind stress, which provides a favorable condition for El Niño onset. Once El Niño reaches its peak at 6 months, the MJO activity and related WWB continue to intensify, possibly through the MJO-ENSO coupled processes[33].

What causes the MJO to become active in the western Pacific after a volcanic eruption?

To understand the processes responsible for the enhanced MJO activity over the western Pacific, we adopt the moisture mode hypothesis[32–37]. Recent theoretical, observational, and modeling studies have collectively demonstrated that the background moisture distribution in the Indo-Pacific warm pool is closely linked to MJO activity. In particular, the increased horizontal advection of background mean moisture to the east, caused by MJO circulation, and the decreased moisture advection to the west of the MJO convective phase together create favorable conditions for the MJO to propagate eastward across the MC[32–37].

Supplementary Fig. 3A shows that, after the volcanic eruption, sharp drying not only occurs over the MC as observed but also to the north of the maximum moisture region in the Indo-Pacific warm pool. The decrease in moisture poleward of the climatological maximum steepens the poleward meridional moisture gradient in both hemispheres. At the same time, the relative wetting in the equatorial central Pacific decreases the zonal moisture gradient (Fig. 2 and Supplementary Fig. 3A). The volcanically-driven stronger meridional moisture gradient over the Indo-Pacific warm pool and weaker zonal moisture gradient near the dateline together favor the eastward propagation of the MJO. To demonstrate this, Fig. 4 compares the lag composites of the MJO-filtered outgoing longwave radiation (OLR) and zonal wind at 850 hPa (U850) in the tropical belt. In the composite of the VE clusters, MJO convection and circulation couplet over the Indian Ocean propagates eastward and enters the western Pacific, thus contributing to the enhanced MJO activity over the western Pacific (Fig. 4A). In the nonVE cluster, however, the MJO convection and circulation signals move slowly eastward and are confined to a narrower longitudinal band with weaker amplitude than in the VE cluster (Fig. 4B). This

https://doi.org/10.1038/s41467-025-56692-2

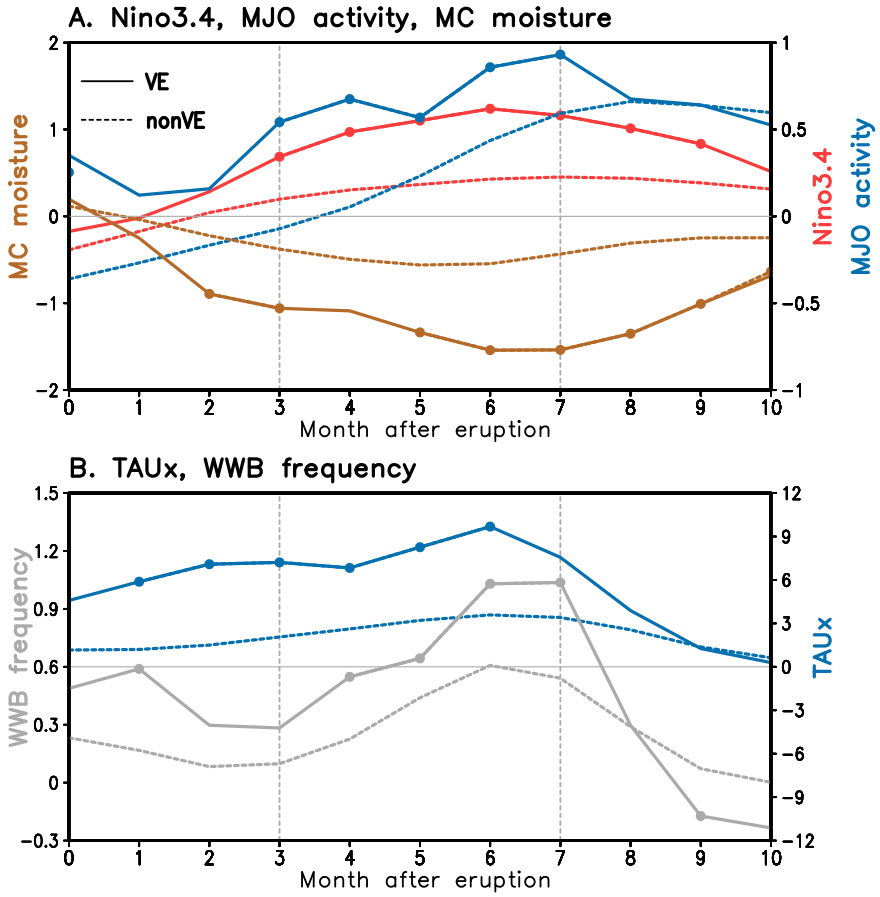


Fig. 3 | Responses of the variables to volcanic eruptions (VEs) with initially neutral El Niño-Southern Oscillation (ENSO) conditions. Averaged monthly time series of (**A**) Maritime Continent (MC) moisture (brown line, left *y*-axis), Madden–Julian oscillation (MJO) activity (blue line, right *y*-axis), Nino 3.4 index (red line, right *y*-axis) and (**B**) westerly wind bursts (WWB) frequency indices (gray line, left *y*-axis) and westerly wind stress (TAUx, blue line, right *y*-axis) from the CESM2-SE for VE (solid line) and nonVE (dashed line) clusters. Month 0 indicates the pre-eruption month, and dashed vertical lines indicate 3 and 7 months after the eruption. Dots indicate months when the difference between the VE and nonVE clusters is statistically significant at the 95% confidence level based on 1000-sample bootstrapping.

demonstrates that the enhanced MJO activity in the western Pacific after the VE is partly attributable to a more coherent eastward propagating signal from the Indian Ocean into the western Pacific.

To understand the key processes associated with the propagation of the MJO, we conducted a moisture budget analysis (Fig. 4C, see "Methods" for details). While moisture to the east of the MJO convection center is enhanced in both the VE and nonVE clusters, the VE cluster shows about 71% greater moisture tendency compared to nonVE (Fig. 4C). The increased moisture tendency explains the more coherent eastward propagation of the MJO in the VE cluster. Both zonal and meridional moisture advection terms are larger in the VE than in the nonVE clusters (Fig. 4C). The zonal moisture advection term is about 5.5 times larger, and meridional moisture advection term is about 1.5 times larger in VE than nonVE cluster. By decomposing the moisture horizontal advection terms, the zonal and meridional advection of the background mean moisture due to the anomalous MJO wind is found to be the most dominant process (Fig. 4C and Supplementary Fig. 4), which is consistent with previous studies[32–37]. Note that the influence of the upper-tropospheric background wind may play a significant role in shaping the dynamics of MJO propagation[38].

In summary, because the area poleward of maximum background moisture over the Indo-Pacific warm pool becomes drier and the area east of the maximum moisture becomes wetter after a VE, these changes together provide favorable conditions for the MJO to propagate further eastward. The enhanced MJO activity over the western Pacific and associated WWBs eventually support the immediate onset of El Niño.

Discussion

Although the volcanically forced ENSO signal has been widely studied, its connection to the MJO has been overlooked in existing studies. Identifying a robust mechanism for the volcanically-forced ENSO has been challenging partly due to systematic model biases, such as the 1-2 years delayed El Niño response after a VE compared to the observed. This study proposes a mechanism based on the central role of the MJO in the immediate onset of an El Niño using the CESM2 single-forcing and large-ensemble simulations and reveals the dynamic processes involved. Because the areas poleward of the maximum seasonal mean moisture dry faster after a tropical volcanic eruption, the background moisture distribution becomes favorable for the MJO to propagate eastward and reach the western Pacific. This increases the likelihood of MJO activity in the western Pacific by about 35% compared to the non-volcanic years, which then increases the westerly wind stress and WWB frequency by ~ 62% and 76%, respectively. These changes eventually enhance the probability of the onset of an El Niño by about 98% after the El Chichón and Mt. Pinatubo eruptions.

Although the CESM2 reasonably simulates the MJO, ENSO, and the immediate onset of El Niño to volcanic forcing compared with many contemporary GCMs, the conclusions from this study are limited to a single model. To examine whether the proposed mechanism is simulated by other models, the same analysis is performed with the large-

https://doi.org/10.1038/s41467-025-56692-2

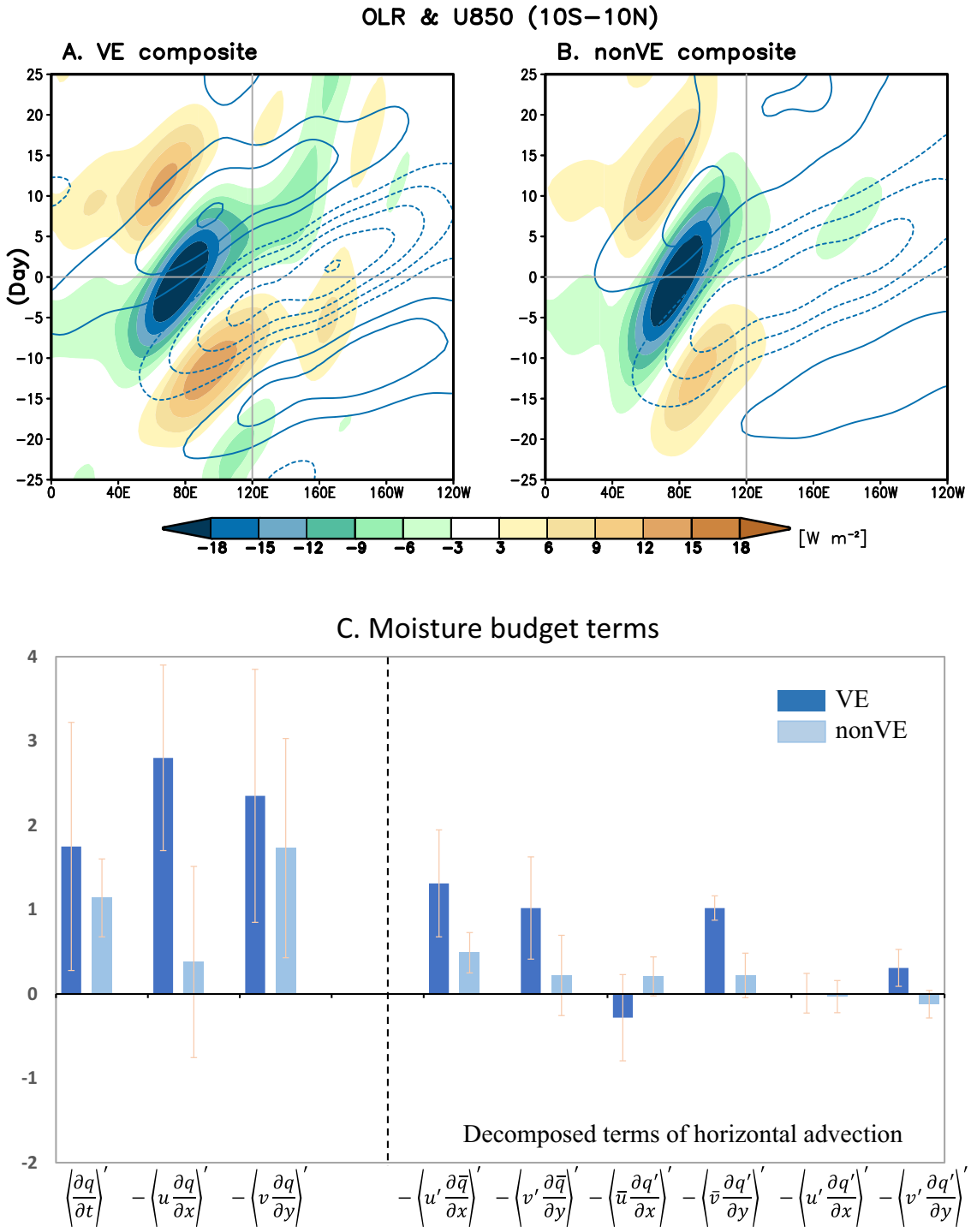


Fig. 4 | Longitude-time evolution of the Madden–Julian oscillation (MJO) and moisture budget terms. A, **B** The lag composites of MJO-filtered Outgoing Longwave Radiation (OLR) (W m^{-2}, shading) and U850 (m s^{-1}, contour interval 0.5, starting at 0.3) averaged over the tropics (10°S–10°N) for the 3–7 months after the volcanic eruption (VE) and nonVE events. Gray solid lines indicate a lag of 0 days and 120°E. **C** Decomposed terms of horizontal moisture advection averaged east of the Maritime Continent (MC) (100°E–160°E, 20°S–15°N, indicated by the box in Supplementary Fig. 4) and over − 2 to 2 days during the VE (dark blue) and nonVE (light blue) events. Units are 10^{-6} kg m^{-2} s^{-1}. The orange whiskers represent the spread of ensemble members, outlining ± 1.0 standard deviation for each term.

ensemble (50 ensemble members) simulation of the HadGEM3 volcanic forcing experiment (see "Methods"). Although the MC moisture is continuously reducing after VE, it reaches its minimum about 10 months after the VE (Supplementary Fig. 5), slower than the observation and CESM2. The MJO activity does not significantly increase and ENSO remains in a neutral state even up to 17 months. This may be partly due to HadGEM3's inability to simulate the key processes related to the MJO dynamics. The slower MC drying and weaker MJO activity over the western Pacific may not be sufficient to enhance WWB activity and trigger the onset of El Niño. We conclude that the realistic response of the MJO associated with MC drying in CESM2 is likely one of the reasons for the immediate onset of El Niño after an eruption. While two state-of-the-art GCMs were analyzed, reaffirming the volcanically forced MJO–ENSO link in a multi-model

framework, such as the Model Intercomparison Project on the climate response to Volcanic Forcing (VolMIP)[6], may help confirm our hypothesis and reduce uncertainty caused by model biases. In particular, we showed that the immediate onset of El Niño is simulated well by the CESM2, whereas most GCMs produce a response with a lag of 1–2 years. The extent to which the model's MJO fidelity contributes to resolving this issue needs to be addressed within a multi-model framework.

A few recent studies have suggested that the suppression of the Northern Africa (NAFR) monsoon plays a primary role in the development of El Niño[16,17]. To test the relative importance of the volcanically-forced drying over the MC versus NAFR in the development of El Niño, ensemble clustering of CESM2-SE is performed using thresholds for MC drying and NAFR drying indices, similar to the results above (Supplementary Fig. 6, see "Methods"). When the MC is relatively dry at the time of the eruption, the MC drying continues, and Niño 3.4 index reaches its maximum after about 6-7 months, similar to the main results shown in this study (Fig. 3). When ensembles are clustered by NAFR drying index, NAFR continues drying until 3 months after the eruption but then tends to increase. The Niño 3.4 index increases but with a weaker magnitude compared with MC dry clustering. Our results, therefore, demonstrate that the MC drying mechanism plays a larger role than NAFR drying in the immediate onset of El Niño after VE in CESM2-SE. In the studies that emphasized the role of NAFR drying[16,17], El Niño develops not in the year the VE occurred, but in the following year. Additionally, one of these studies[17] showed an immediate El Niño onset after VE when the MC region was cooled (their *MCext* experiment). Therefore, it appears that the MC drying is largely responsible for the immediate El Niño onset after VE, while NAFR drying plays a dominant role in the delayed El Niño response. It is worth noting that the GCM used in Pausata et al. (2023) has a reasonable MJO simulation capability[39], which may suggest our MJO-mediated, volcanically forced El Niño onset mechanism played a role in the immediate El Niño onset after VE in their MCext experiment as well.

While we suggest that reasonable simulation of the MJO in CESM2 plays a central role, some studies have indicated that the ocean dynamical thermostat (ODT) effect is also important for spurring westerly anomalies and contributing to the quick onset of El Niño. The ODT has been shown to work well in some theoretical models[40,41] while lacking in others[16]. As with most GCMs, the ODT effect is found to be weak in CESM2 possibly due to the biases of equatorial Pacific upwelling[42]. Therefore, the ODT effect may not play a central role in this study.

Our findings have important implications for future climate change and geoengineering. Among various solar geoengineering techniques, the stratospheric aerosol injection method is sometimes described as a "man-made volcano" because it aims to mimic large volcanic eruptions by injecting sulfate aerosols into the stratosphere to offset the effects of anthropogenic warming[43]. However, the potential risks to the environment, particularly concerning the global hydrological cycle (e.g., severe droughts and extreme precipitation), remain highly uncertain[5]. Understanding the potential mechanisms behind these changes is crucial. In addition, because the MJO and ENSO are projected to be amplified due to greenhouse warming in the future[44,45], Pinatubo-like volcanoes or solar geoengineering could alter the MJO–ENSO response, adding another layer of complexity and uncertainty to our understanding of how climate change will progress.

Methods

Model experiments and data

We use the historical simulations of the Community Earth System Model Version 2.0 single-forcing large ensemble (CESM2-SE) experiments[46]. The CESM2 reasonably simulates both the basic state and modes of tropical variabilities, such as the ENSO and MJO[30–34,47]. The CESM2-SE offers a unique opportunity to quantify the relative contributions of anthropogenic and natural forcings to the evolution of the Earth system. To investigate the influence of volcanic forcing, the "EE2" experiment is analyzed, which consists of 15 members that run from 1850 to 2050 where forcings from greenhouse gases, anthropogenic aerosol, and biomass-burning aerosol are held fixed at 1850s value and forcings from "everything else" in CESM2 (EE2) are evolving. The EE2 forcing experiment includes forcing from solar insolation, stratospheric volcanic aerosol, stratospheric and tropospheric ozone, and land-use and land-cover change. Among these, the volcanic forcing has been shown to have the largest impact on the year-to-year variation of surface temperature during the historical period[46]. Therefore, to disentangle the impact of volcanic forcing on MJO and ENSO, 15 ensemble members from the EE2 experiment from 1980 to 2014 are analyzed. Supplementary Fig. 7 shows the monthly mean stratospheric aerosol optical depth (AOD) at 550 nm from the Whole Atmosphere Community Climate Model Version 6 (WACCM6) that produced the volcanic aerosol forcing[46]. The AOD exceeds 0.06 during two volcanic eruptions, El Chichón in 1982 and Mt. Pinatubo in 1991 (Supplementary Fig. 7)

To verify the results obtained from the CESM2-SE, CESM2 large-ensemble (CESM2-LE) simulations are compared[30]. Although volcanic forcing cannot be isolated from other external forcings, CESM2-LE offers a unique opportunity for analyzing the forced responses as it consists of 100 ensemble members. We utilize all 100 ensemble members during the same period as CESM2-SE, from 1980 to 2014.

To test the hypothesis drawn from CESM2-SE and CESM2-LE, the hypothesis is further examined with HadGEM3-GC3.1-LL single forcing large ensemble experiment (hereafter referred to as HadGEM3). The HadGEM3-GC3 reasonably simulates the MJO[39]. The HadGEM3 historical volcanic-forcing simulation[48], driven by volcanic forcing only, is analyzed from 1980 to 2014 using a similar approach applied in the CESM2 analysis. Fifty ensemble members are analyzed. Note that some output variables are not available for download in HadGEM3, such as daily westerly wind stress.

Daily and monthly mean zonal wind and specific humidity are obtained from the European Center for Medium-Range Weather Forecasting (ECMWF) Interim Reanalysis[49]. The monthly mean SST comes from the National Oceanic and Atmospheric Administration (NOAA) Optimum Interpolation SST V2[50]. The OLR data is from the NOAA Advanced Very High-Resolution Radiometer[51]. The monthly sea surface height (SSH) is obtained from the ECMWF Ocean Reanalysis System 4[52]. For brevity, the reanalysis and satellite data sets are referred to as observations. All observations and simulations are interpolated onto a 2.5° longitude and 2.5° latitude grid. Monthly and daily anomalies are calculated by subtracting the climatology of the 1980–2014 period for both the observations and simulations. The possible impact of anthropogenic forcing is removed through linear detrending.

Volcanic eruption events and the analysis window

The Northern Hemisphere and tropical eruptions tend to favor El Niño-like conditions, while Southern Hemisphere eruptions enhance the probability of La Niña-like events[16,29]. In addition, only VEs that are strong enough to inject aerosols into the stratosphere and that pass a certain threshold (i.e., absolute radiative forcing greater than 3.3 W/m^2) can increase the probability of an El Niño event occurring[53]. Since the satellite era, only two eruptions in the tropics have surpassed this threshold: El Chichón in Mexico (93°W, 17°N) in April 1982 and Mt. Pinatubo in the Philippines (120°E, 15°N) in June 1991. The plumes from El Chichón reached about 31 km at their highest point and released ~ 7.5 Tg of SO_2, while Mt. Pinatubo reached 40 km and injected ~ 20 Tg of SO_2, both exceeding volcanic explosivity index category 5[1]. Notably, both eruptions occurred at tropical latitudes. We define the month of eruption (month 0) as April 1982 and June 1991, respectively.

Therefore, the period three to seven months after the VE, which is the window of analysis in the present study, corresponds to July to November 1982 for El Chichón and September 1991 to January 1992 for Mt. Pinatubo. The non-VE years are defined as the years from 1980 to 2014, excluding 1982 and 1991, unless otherwise noted.

Indices

Seven indices are defined in this study: MJO activity index, Maritime Continent (MC) moisture index, northern African (NAFR) moisture index, westerly wind stress (TAUx) index, WWB frequency index, recharge index, and Niño 3.4 index. For our purposes, an intraseasonal filter is applied to retain only eastward propagating signals of wavenumbers 0–9 with periods between 30 and 96 days[54]. This is hereafter referred to as the "MJO-filter". The MJO activity is defined as the monthly standard deviation of the MJO-filtered daily OLR. The MJO activity index is then defined as the monthly MJO activity anomalies averaged over 140°E–200°E and 15°S–15°N (indicated by the blue boxes in Fig. 2C and D). The MC moisture index is defined as the monthly moisture anomalies averaged over 90°E–150°E and 15°S–15°N (indicated by the brown boxes in Fig. 2A and B). The NAFR moisture index is defined as the monthly moisture anomalies averaged over 20°W–50°E and 10°S–30°N.

The westerly wind stress index (hereafter TAUx) is defined as the monthly mean zonal wind stress anomalies averaged over 130°E–200°E and 5°S–5°N (indicated by the box in Supplementary Fig. 3C). The WWB frequency index is defined as the number of days when daily surface zonal wind stress anomaly averaged over tropical western Pacific (130°E-200°E, 5°S-5°N) exceeds 1.0σ for three consecutive days, indicating a sustained surface westerly. The daily frequency is then counted over a month to define the monthly WWB frequency index. Note that the definition of WWBs is loosely analogous to that used by Santoso et al[55]. but not as strict as other definitions[56].

The recharge index is defined as the monthly SSH anomaly averaged over the western tropical Pacific (120°E–205°E, 5°S–5°N)[31]. Based on the delayed oscillator and recharge–discharge oscillator paradigm for the ENSO[57], the equatorial Pacific Ocean heat content is regarded as a key precursor to the ENSO. Equatorial ocean heat accumulates (or recharges) about three to six months before the onset of El Niño and then discharges during and after El Niño. In particular, the recharge in the western Pacific is accompanied by a higher sea level associated with a deeper thermocline[58]. Thus SSH is often used as a proxy for ocean heat variation. The recharge–discharge process for ENSO is well-simulated in the CESM2[31]. The Niño 3.4 index is calculated using the relative SST (RSST)[59] averaged over the Niño 3.4 region (190°E–240°E and 5°S–5°N, the box in Supplementary Fig. 3D). RSST is defined as the SST signal after removing the tropical (20°S–20°N) mean SST anomalies because it better highlights the intrinsic ENSO signal after a volcanic eruption[15,17].

Ensemble clustering for the VE and nonVE groups and composite analysis

We subsample the ensemble members by considering each ensemble's recharge phase in the pre-eruption month (month 0) into account and select those ensembles that are within a similar range as the observed recharge phase. Given that the two eruptions occurred in April (El Chichón) and June (Mt. Pinatubo), and by considering the seasonal phase locking of the ENSO, we use the April-May-June (AMJ) averaged normalized recharge index as the threshold for ensemble clustering. The observed AMJ recharge index is 0.9σ and 0.2σ for El Chichón and Mt. Pinatubo, respectively, indicating neutral ENSO conditions before both volcanic eruptions. Therefore, ensemble members are selected if the normalized AMJ recharge index ranges between 0.2σ and 0.9σ, coinciding with the observed recharge phase. About 53% of ensembles are selected as VE clusters during VE years and 25% as nonVE clusters during nonVE years. Note that, due to the phase locking of ENSO, the composites of the mean state (Supplementary Fig. 3) are calculated for the September-October-November (SON) average.

For the daily lag composite analysis (Fig. 4), a reference time series is first defined as the area-averaged MJO-filtered OLR anomalies over the Indian Ocean (80°E–110°E and 15°S–15°N). The lag composite is calculated when the reference time series from each clustered ensemble is below −1.0σ and has the minimum values between −1 and +1 day. Both monthly and daily composite analyses are conducted over the 3–7-month window for both the VE and nonVE clusters starting from AMJ.

To further assess the relative contribution of MC drying and NAFR drying on the onset of El Niño, we subsample the ensemble members by taking each ensemble's MC index and NAFR index in the pre-eruption month (month 0) into account and select those ensembles that are less than −1.0σ, indicating strong drying over each continent right before the volcanic eruptions.

Moisture budget analysis

To explain the key processes involved in MJO propagation (Fig. 4C), the following column-integrated moisture budget equation is utilized:

$$\langle \frac{\partial q}{\partial t} \rangle' = -\langle u \frac{\partial q}{\partial x} \rangle' - \langle v \frac{\partial q}{\partial y} \rangle' - \langle \omega \frac{\partial q}{\partial p} \rangle' - P' + E' \quad (1)$$

where q, u, v, ω, P, and E are the specific humidity, zonal wind, meridional wind, vertical wind, precipitation, and evaporation, respectively. The angled bracket indicates a mass-weighted vertical integral and the prime denotes MJO-filtered anomalies. We focus on the tendency term and horizontal (zonal and meridional) advection terms because the horizontal advection processes are key to MJO eastward propagation[36,37]. The first three terms (the moisture tendency term and zonal and meridional advection terms) are calculated using the daily CESM2-SE output, whereas the sum of the other terms, which is often referred to as column processes[60], is obtained as the residual. Note that the role of column processes on the MJO is non-negligible and warrants further analysis. Changes in moisture advection could be attributed to changes in the background mean moisture distribution, anomalous MJO circulation or the nonlinear interaction between the two. To further understand the contribution of the mean state and the MJO to the key processes in the dominant term, the moisture advection terms are decomposed into different timescale interactions as follows:

$$\begin{aligned} -\left\langle u \frac{\partial q}{\partial x} \right\rangle' - \left\langle v \frac{\partial q}{\partial y} \right\rangle' \cong & -\left\langle u' \frac{\partial \bar{q}}{\partial x} \right\rangle' - \left\langle v' \frac{\partial \bar{q}}{\partial y} \right\rangle' - \left\langle \bar{u} \frac{\partial q'}{\partial x} \right\rangle' \\ & - \left\langle \bar{v} \frac{\partial q'}{\partial y} \right\rangle' - \left\langle u' \frac{\partial q'}{\partial x} \right\rangle' - \left\langle v' \frac{\partial q'}{\partial y} \right\rangle' + h.o.t \end{aligned} \quad (2)$$

where the overbar represents the background mean (September-October-November average after volcanic eruptions). Moisture budget terms are averaged from a lag of −2 to +2 days over the western Pacific (100°E–160°E, 20°S–15°N, as indicated by the boxes in Supplementary Fig. 4).

Confidence interval

The confidence interval for the results shown in Fig. 3 and Supplementary Fig. 3 is calculated using the bootstrap method. First, the anomaly composite is constructed by selecting random years from the entire period (1980–2014) with the same number of VE (2 years) and nonVE groups (33 years) with initially neutral ENSO conditions in AMJ without overlapping years. The anomalies are then calculated between the sampled VE and nonVE groups, respectively. The difference between the VE and nonVE group composites is then calculated.

This process is repeated 1000 times with replacement to obtain a probability distribution function of the differences. The 2.5th and 97.5th percentile values are then used to define the 95% confidence interval.

Data availability

Data related to this paper can be downloaded from ERA-Interim, https://www.ecmwf.int/en/forecasts/datasets/reanalysis-datasets/era-interim; ECMWF ORAS4, https://www.ecmwf.int/en/forecasts/dataset/ocean-reanalysis-system-4; NOAA OLR, https://www.esrl.noaa.gov/psd/data/gridded/data.interp_OLR.html; NOAA OI SST V2, https://psl.noaa.gov/data/gridded/data.noaa.oisst.v2.html; CESM2 single forcing large ensemble, https://www.cesm.ucar.edu/working-groups/climate/simulations/cesm2-single-forcing-le; CESM2 large ensemble, https://www.cesm.ucar.edu/community-projects/lens2; HadGEM3 simulations, https://esgf-node.llnl.gov/search/cmip6/. The processed data is accessible on the Zenodo repository under https://doi.org/10.5281/zenodo.14607607.

Code availability

The codes used in this study are accessible on the Zenodo repository under https://doi.org/10.5281/zenodo.14607607.

References

1. Sellitto, P. et al. The unexpected radiative impact of the Hunga Tonga eruption of 15th January 2022. *Commun. Earth Environ.* **3**, 288 (2022).
2. The World Bank, "January 15, 2022 Hunga Tonga-Hunga Ha'api Eruption and Tsunami, Tonga" (Global Rapid Post Disaster Damage Estimation Report (2022).
3. Aquila, V. et al. Impacts of the eruption of Mount Pinatubo on surface temperatures and precipitation forecasts with the NASA GEOS subseasonal-to-seasonal system. *J. Geophys. Res. Atmos.* **126**, e2021JD034830 (2021).
4. Robock, A. & Mao, J. The volcanic signal in surface temperature observations. *J. Clim.* **8**, 1086–1103 (1995).
5. Hegerl, G. C. & Solomon, S. Risks of climate engineering. *Science* **325**, 955–956 (2009).
6. Zanchettin, D. et al. The model intercomparison project on the climatic response to Volcanic forcing (VolMIP): experimental design and forcing input data for CMIP6. *Geosci. Model Dev.* **9**, 2701–2719 (2016).
7. Dee, S. G. et al. No consistent ENSO response to volcanic forcing over the last millennium. *Science* **367**, 1477–1481 (2020).
8. Brad Adams, J., Mann, M. E. & Ammann, C. M. Proxy evidence for an El Niño-like response to volcanic forcing. *Nature* **426**, 274–278 (2003).
9. Robock, A. Comment on "No consistent ENSO response to volcanic forcing over the last millennium. *Science* **369**, eabc0502 (2020).
10. McGregor, S. et al. in *El Niño Southern Oscillation in a Changing Climate*. (2020).
11. Ding, Y. et al. Ocean response to volcanic eruptions in Coupled Model Intercomparison Project 5 simulations. *J. Geophys. Res. Oceans* **119**, 5622–5637 (2014).
12. McGregor, S. & Timmermann, A. The effect of explosive tropical volcanism on ENSO. *J. Clim.* **24**, 2178–2191 (2011).
13. Ohba, M., Shiogama, H., Yokohata, T. & Watanabe, M. Impact of strong tropical volcanic eruptions on ENSO simulated in a coupled GCM. *J. Clim.* **26**, 5169–5182 (2013).
14. Predybaylo, E., Stenchikov, G. L., Wittenberg, A. T. & Zeng, F. Impacts of a Pinatubo-size volcanic eruption on ENSO. *J. Geophys. Res. Atmos.* **122**, 925–947 (2017).
15. Paik, S., Min, S.-K., Iles, C. E., Fischer, E. M. & Schurer, A. P. Volcanic-induced global monsoon drying modulated by diverse El Nino responses. *Sci. Adv.* **6**, eaba1212 (2020).
16. Pausata, F. S. R., Zhao, Y., Zanchettin, D., Caballero, R. & Battisti, D. S. Revisiting the mechanisms of ENSO response to tropical volcanic eruptions. *Geophys. Res. Lett.* **50**, e2022GL102183 (2023).
17. Khodri, M. et al. Tropical explosive volcanic eruptions can trigger El Niño by cooling tropical Africa. *Nat. Commun.* **8**, 778 (2017).
18. Bjerknes, J. Atmospheric teleconnections from the equatorial Pacific. *Mon. Weather Rev.* **97**, 163–172 (1969).
19. Seiki, A. & Takayabu, Y. N. Westerly wind bursts and their relationship with intraseasonal variations and ENSO. Part I: statistics. *Mon. Weather Rev.* **135**, 3325–3345 (2007).
20. Kiladis, G. N., Meehl, G. A. & Weickmann, K. M. Large-scale circulation associated with westerly wind bursts and deep convection over the western equatorial Pacific. *J. Geophys. Res. Atmos.* **99**, 18527–18544 (1994).
21. McPhaden, M. J. Genesis and evolution of the 1997-98 El nino. *Science* **283**, 950–954 (1999).
22. Harrison, D. E. & Schopf, P. S. Kelvin-wave-induced anomalous advection and the onset of surface warming in El Niño events. *Mon. Weather Rev.* **112**, 923–933 (1984).
23. Eddebbar, Y. A. et al. El Niño–like physical and biogeochemical Ocean response to tropical eruptions. *J. Clim.* **32**, 2627–2649 (2019).
24. Madden, R. & Julian, P. Further evidence of global-scale, 5-day pressure waves. *J. Atmos. Sci.* **29**, 1464 (1972).
25. Puy, M., Vialard, J., Lengaigne, M. & Guilyardi, E. Modulation of equatorial Pacific westerly/easterly wind events by the Madden–Julian oscillation and convectively-coupled Rossby waves. *Clim. Dyn.* **46**, 2155–2178 (2016).
26. Hendon, H. H., Wheeler, M. C. & Zhang, C. Seasonal dependence of the MJO–ENSO relationship. *J. Clim.* **20**, 531–543 (2007).
27. Kessler, W. S., McPhaden, M. J. & Weickmann, K. M. Forcing of intraseasonal Kelvin waves in the equatorial Pacific. *J. Geophys. Res. Oceans* **100**, 10613–10631 (1995).
28. Chiodi, A. M., Harrison, D. E. & Vecchi, G. A. Subseasonal atmospheric variability and El Niño waveguide warming: Observed effects of the Madden–Julian oscillation and westerly wind events. *J. Clim.* **27**, 3619–3642 (2014).
29. Ward, B., Pausata, F. S. R. & Maher, N. The sensitivity of the El Niño–Southern oscillation to volcanic aerosol spatial distribution in the MPI Grand Ensemble. *Earth Syst. Dynam.* **12**, 975–996 (2021).
30. Rodgers, K. B. et al. Ubiquity of human-induced changes in climate variability. *Earth Syst. Dynam.* **12**, 1393–1411 (2021).
31. Capotondi, A., Deser, C., Phillips, A. S., Okumura, Y. & Larson, S. M. ENSO and Pacific decadal variability in the community earth system model version 2. *J. Adv. Model. Earth Syst.* **12**, e2019MS002022 (2020).
32. Ahn, M.-S. et al. MJO Propagation across the maritime continent: Are CMIP6 models better than CMIP5 models? *Geophys. Res. Lett.* **47**, e2020GL087250 (2020).
33. Kang, D. et al. The role of the mean state on MJO simulation in CESM2 ensemble simulation. *Geophys. Res. Lett.* **47**, e2020GL089824 (2020).
34. Back, S. et al. MJO Diversity in CMIP6 models. *J. Clim.* **37**, 4835–4850 (2024).
35. Sobel, A. & Maloney, E. Moisture modes and the eastward propagation of the MJO. *J. Atmos. Sci.* **70**, 187–192 (2013).
36. Adames, A. F. & Kim, D. The MJO as a dispersive, convectively coupled moisture wave: Theory and observations. *J. Atmos. Sci.* **73**, 913–941 (2016).
37. Jiang, X. et al. Fifty years of research on the madden-julian oscillation: Recent progress, challenges, and perspectives. *J. Geophys. Res. Atmos.* **125**, e2019JD030911 (2020).
38. Roundy, P. E. Role of dry dynamics in the maritime continent barrier effect in the Madden–Julian oscillation. *J. Atmos. Sci.* **81**, 2041–2050 (2024).

39. Ahn, M.-S. et al. MJO simulation in CMIP5 climate models: MJO skill metrics and process-oriented diagnosis. *Clim. Dyn.* **49**, 4023–4045 (2017).
40. Mann, M. E., Cane, M. A., Zebiak, S. E. & Clement, A. Volcanic and solar forcing of the tropical Pacific over the past 1000 years. *J. Clim.* **18**, 447–456 (2005).
41. Predybaylo, E. et al. El Niño/Southern oscillation response to low-latitude volcanic eruptions depends on ocean pre-conditions and eruption timing. *Commun. Earth Environ.* **1**, 12 (2020).
42. Fu, S. et al. Historical changes in wind-driven ocean circulation drive pattern of Pacific warming. *Nat. Commun.* **15**, 1562 (2024).
43. Robock, A. Albedo enhancement by stratospheric sulfur injections: More research needed. *Earth's Future* **4**, 644–648 (2016).
44. Cai, W. et al. Changing El Niño–Southern oscillation in a warming climate. *Nat. Rev. Earth Environ.* **2**, 628–644 (2021).
45. Roxy, M. K. et al. Twofold expansion of the Indo-Pacific warm pool warps the MJO life cycle. *Nature* **575**, 647–651 (2019).
46. Simpson, I. R. et al. The CESM2 single-forcing large ensemble and comparison to CESM1: Implications for experimental design. *J. Clim.* **36**, 5687–5711 (2023).
47. Danabasoglu, G. et al. The community earth system model version 2 (CESM2). *J. Adv. Model. Earth Syst.* **12**, e2019MS001916 (2020).
48. Gillett, N. P. et al. The detection and atribution model intercomparison project (DAMIP v1.0) contribution to CMIP6. *Geosci. Model Dev.* **9**, 3685–3697 (2016).
49. Dee, D. P. et al. The ERA-Interim reanalysis: configuration and performance of the data assimilation system. *Q. J. R. Meteorol. Soc.* **137**, 553–597 (2011).
50. Reynolds, R. W., Rayner, N. A., Smith, T. M., Stokes, D. C. & Wang, W. An improved in situ and satellite SST analysis for climate. *J. Clim.* **15**, 1609–1625 (2002).
51. Liebmann, B. & Smith, C. A. Description of a complete (Interpolated) outgoing longwave radiation dataset. *Bull. Am. Meteorol. Soc.* **77**, 1275–1277 (1996).
52. Balmaseda, M. A., Mogensen, K. & Weaver, A. T. Evaluation of the ECMWF ocean reanalysis system ORAS4. *Q. J. R. Meteorol. Soc.* **139**, 1132–1161 (2013).
53. Emile-Geay, J., Seager, R., Cane, M. A., Cook, E. R. & Haug, G. H. Volcanoes and ENSO over the past millennium. *J. Clim.* **21**, 3134–3148 (2008).
54. Kiladis, G. N., Straub, K. H. & Haertel, P. T. 2005: Zonal and vertical structure of the Madden–Julian oscillation. *J. Atmos. Sci.* **62**, 2790–2809 (2005).
55. Santoso, A., Mcphaden, M. J. & Cai, W. The defining characteristics of ENSO extremes and the strong 2015/2016 El Niño. *Rev. Geophys.* **55**, 1079–1129 (2017).
56. Harrison, D. E. & Vecchi, G. A. Westerly wind events in the tropical Pacific, 1986–95. *J. Clim.* **10**, 3131–3156 (1997).
57. Jin, F.-F. An equatorial Ocean recharge paradigm for ENSO. Part I: Conceptual model. *J. Atmos. Sci.* **54**, 811–829 (1997).
58. Meinen, C. S. & McPhaden, M. J. Observations of warm water volume changes in the equatorial Pacific and their relationship to El Niño and La Niña. *J. Clim.* **13**, 3551–3559 (2000).
59. Vecchi, G. A. & Soden, B. J. Effect of remote sea surface temperature change on tropical cyclone potential intensity. *Nature* **450**, 1066–1070 (2007).
60. Chikira, M. Eastward-propagating intraseasonal oscillation represented by Chikira–Sugiyama Cumulus parameterization. Part II: Understanding moisture variation under weak temperature gradient balance. *J. Atmos. Sci.* **71**, 615–639 (2014).

Acknowledgements

H.K. was supported by the National Research Foundation of Korea (NRF) grant funded by the Korean government (NRF-RS-2023-00278113) and NOAA Grant NA22OAR4590168. S.K.M. was supported by an NRF grant funded by the Korean government (NRF2021R1A2C3007366). D.K. was supported by the New Faculty Startup Fund and Creative-Pioneering Researchers Program from Seoul National University, the NRF grant funded by the Korea government (NRF-RS-2024-00336160), and NOAA grant NA22OAR4310608.

Author contributions

H.K. and S.K.M. initiated and designed the research and wrote the draft manuscript. H.K. analyzed the data and generated the figures. D.K. and D.V. discussed the results and contributed to writing the manuscript.

Competing interests

The authors declare no competing interests.

Additional information

Supplementary information The online version contains supplementary material available at https://doi.org/10.1038/s41467-025-56692-2.

Correspondence and requests for materials should be addressed to Hyemi Kim or Seung-Ki Min.

Peer review information *Nature Communications* thanks Achmad Yasir Baeda, Hien Bui, Paul Roundy, and the other anonymous reviewers for their contribution to the peer review of this work. A peer review file is available.

Reprints and permissions information is available at http://www.nature.com/reprints

Publisher's note Springer Nature remains neutral with regard to jurisdictional claims in published maps and institutional affiliations.

Open Access This article is licensed under a Creative Commons Attribution-NonCommercial-NoDerivatives 4.0 International License, which permits any non-commercial use, sharing, distribution and reproduction in any medium or format, as long as you give appropriate credit to the original author(s) and the source, provide a link to the Creative Commons licence, and indicate if you modified the licensed material. You do not have permission under this licence to share adapted material derived from this article or parts of it. The images or other third party material in this article are included in the article's Creative Commons licence, unless indicated otherwise in a credit line to the material. If material is not included in the article's Creative Commons licence and your intended use is not permitted by statutory regulation or exceeds the permitted use, you will need to obtain permission directly from the copyright holder. To view a copy of this licence, visit http://creativecommons.org/licenses/by-nc-nd/4.0/.

© The Author(s) 2025